atmosphere

MDPI

Article

Analysis of the Micro-Physical Characteristics of the Sea of Clouds Phenomena in Jiuxian Mountain Based on Multiple Source Observations

Si Cheng [1,2], Zilun Lin [1,*], Jianding Zhou [1], Geng Han [1], Zhenhao Chen [3] and Qingbo Yang [4]

[1] Fujian Quanzhou Meteorological Bureau, Quanzhou 362000, China; chs19870218@126.com (S.C.); zidanefans@126.com (G.H.)
[2] Fujian Key Laboratory of Severe Weather, Fuzhou 350001, China
[3] Fujian Dehua Meteorological Bureau, Quanzhou 362500, China
[4] Fujian Jiuxian Mountain Observatory, Quanzhou 362500, China
* Correspondence: l416352583@163.com

Abstract: The micro-physical characteristics of a typical sea of clouds process in Jiuxian Mountain are investigated by comprehensively analyzing parameters that delineate the micro-physical characteristics of clouds and atmospheric stratification based on data from a cloud radar, wind profiler, meteorological gradient observation in high mountains, and other observations. The results show that water vapor condenses into cloud particles via an entrained and mixing process accompanied by an updraft originating from orographic uplift. During the thickening stage of the sea of clouds, atmospheric motion within the clouds is featured as "downdraft on the top—updraft on the bottom". The zero vertical velocity area is located closely to the maximum of liquid water content. The thermal inversion layer is formed during the maintenance stage; however, the enhancement of inversion on the cloud top could suppress updraft in areas with a high liquid water content. The values mainly concentrate on the cloud top, and repetitively lifting and falling processes caused by the atmospheric upward and downward motion are in favor of the coalescence growth of cloud particles, which result in the persistence of strong radar echo. At the dissipation stage, warming on the cloud top is greater than that on the cloud bottom due to the short-wave absorption of clouds as the solar radiation enhances. As a result, the inversion layer thickens and elevates, evaporation caused by heating outweighs the condensation caused by cooling, a strong radar echo band descends from the top to the middle part of clouds, a sea of clouds dissipates gradually as cloud particles evaporates, and the particle size and concentration number of cloud particles decrease simultaneously.

Keywords: multiple source observations; sea of clouds in high mountains; micro-physicalcharacteristics; cloud radar

Citation: Cheng, S.; Lin, Z.; Zhou, J.; Han, G.; Chen, Z.; Yang, Q. Analysis of the Micro-Physical Characteristics of the Sea of Clouds Phenomena in Jiuxian Mountain Based on Multiple Source Observations. *Atmosphere* **2024**, *15*, 207. https://doi.org/10.3390/atmos15020207

Academic Editors: Feifei Shen and Yunheng Wang

Received: 4 December 2023
Revised: 19 January 2024
Accepted: 23 January 2024
Published: 6 February 2024

1. Introduction

Climatic resources in mountainous areas are one of the most important climatic resources for tourism. Jiuxian Mountain in Dehua County is a famous and historic tourist resort in the south of Fujian Province. Statistically, the average number of foggy days in a year is about 300, and the relative humidity is around 87%. Because of the constant change in weather conditions in mountainous areas, magnificent sceneries, such as seas of clouds and waterfalls of clouds, emerge frequently, which are of great value to the tourist industry [1–4].

The classification of seas of clouds in high mountains and their characteristics have been widely investigated by previous studies [5,6]. However, those studies mainly focused on the influence of large-scale atmospheric circulations and weather conditions on the sea of clouds, due to the lack of more detailed observations like meteorological gradient observation [7]. The phenomenon of a sea of clouds is closely related to local

atmospheric stratification structure; the formation and dissipation of a sea of clouds can be explained more thoroughly by investigating the cloud micro-physical condition and related formation mechanism.

The formation and evolution of clouds are closely related to cloud micro-physical processes [8,9]. Initially, water vapor molecules turn into condensation nuclei through diffusion and evaporation; particles aggregate by coalescence afterwards, and moist air that contains these particles is carried upwardly by atmospheric convection. If the upward air cools down adiabatically in the presence of suitable aerosol particles (condensation nuclei), water vapor would condense or sublimate into liquid or solid cloud particles if the air is supersaturated. Aggregation is the main process that leads to the further growth of cloud particles, which could occur among particles with the same or different thermodynamic phase states [10,11].

The wavelength of HMB-KPS cloud radar is comparable to the scale of cloud particles, with high-level sensitivity and resolution, which could detect the inner structure of the cloud body and is an ideal tool to observe and study non-precipitation clouds, weak precipitation clouds, or fog. The wavelength of cloud radar ranges from 1–10 mm, with a 30–300 GHz frequency. Cloud radar has been used to observe the temporal and spatial evolution of cloud structure and obtain cloud macro-features, such as cloud top, cloud thickness, cloud form, cloud coverage, etc. [12]. Furthermore, the inversed variables, size of cloud particles, number concentration, liquid (ice) water content, etc., can be derived from cloud radar data [13,14], which could be useful to distinguish sea of clouds phenomena in high mountains. In addition, data from wind profilers and meteorological gradient observations also play important roles in studying the change in boundary layer height and turbulence within the boundary layer [15]. They could be used to reveal the distribution characteristics of temperature, humidity, wind speed, and liquid water boundary; compare them with profiles of atmospheric temperature, humidity, and clouds; establish vertical structural models of seas of clouds; etc.

Therefore, based on artificial observation records of the sea of clouds from the Jiuxian Mountain national meteorological station and data from cloud radar, wind profilers, and meteorological gradient observations in high mountains, characteristics of cloud micro-physics and the atmospheric stratification structure of the sea of clouds are exhibited and summarized as meteorological indicators to provide useful guidance for tourism service.

2. Data and Methods

A case of a sea of clouds with wide coverage occurred in Jiuxian Mountain at 0600–0900 Beijing time (BJT) on 10 March 2021. Data adopted in this study are from HMB-KPS (Ka-band) cloud radar (Tables 1 and 2), LC wind profilers, and meteorological gradient observations in high mountains. The locations of these devices and their altitudes are shown in Figure 1.

Table 1. Major performance parameters for HMB-KPS (Ka-band) cloud radar.

Parameter	Value
Operating frequency	35 GHz ± 500 MHz
Beamwidth	0.4°
Pulse repetition rate	5988~16,666 Hz
Peak power	20 W
Detection range	0.12 km~20.07 km
Azimuth angle	0°
Pitch angle	90°
Spatial resolution	30 m
Temporal resolution	1 min
Scan mode (4)	Boundary mode Mid-cloud mode Cirrus mode Precipitation mode

Table 2. Major parameters of 4 detection modes.

Parameter	Boundary Mode	Mid-Cloud Mode	Cirrus Mode	Precipitation Mode
Pulse width (μs)	0.2	8	24	0.2
Pulse repetition rate (Hz)	16,666	8333	5988	5988
Number of coherent accumulations	4	2	1	1
Number of incoherent accumulations	16	32	32	32
Effective height detection (km)	0.12~7.5	1.47~7.5	3.87~20	0.12~20
Maximum no-blur speed (m/s)	8.93	8.93	12.83	12.83
Velocity resolution (cm/s)	6.98	6.98	10.02	10.02

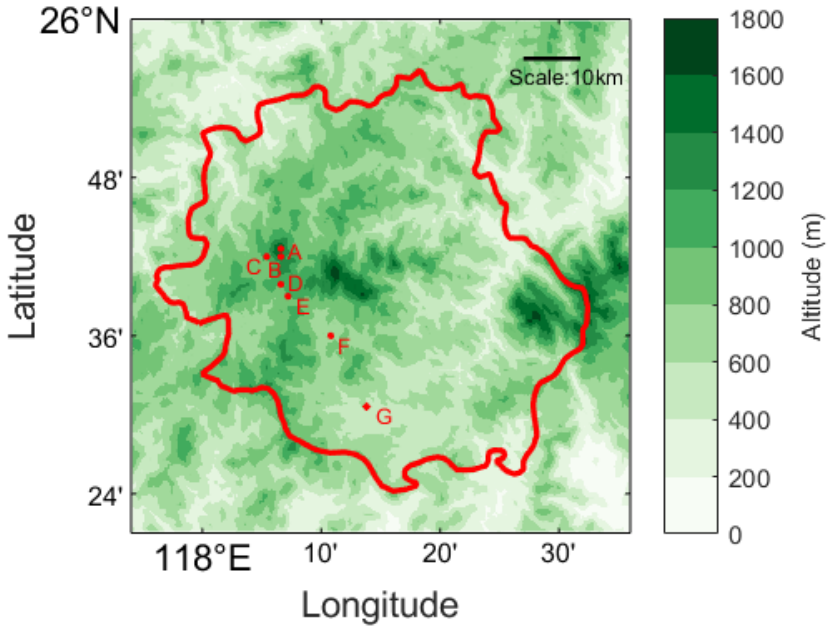

Figure 1. Locations of devices; the red polygon indicates the boundary of Dehua County. Red dots indicate automatic weather stations (altitude: A, 1654 m; B, 1552 m; C, 1336 m; D, 1092 m; E, 920 m; F, 690 m), wind profiler, and Ka-band cloud radar (altitude: G, 645 m).

The temporal resolution of Ka-band cloud radar data is minute-by-minute, the vertical resolution is 30 m, and the maximum height of detection is 20.07 km. The variables directly observed by cloud radar include reflectivity factor Z, Doppler velocity V, velocity spectral width S_W, and so on. The inversed variables are vertical velocity ω, effective radius of cloud particles Re, number concentration N, and liquid water content LWC. The inversion method is described by Equation (1) [8,16]:

$$\beta = \left\{ \frac{\alpha_v^2}{S_w^2} \left[\frac{\Gamma(2b_v+7)}{\Gamma(7)} - \left(\frac{\Gamma(b_v+7)}{\Gamma(7)} \right)^2 \right] \right\}^{1/(2b_v)} \quad (1)$$

Among which, Sw is the velocity spectrum width; β is the slope factor; Γ is the gamma function, defined as $\Gamma(n) = \int_0^\infty x^{n-1}e^{-x}dx$. Given a positive integer, $\Gamma(n) = (n-1)!, \Gamma(1) = 1$. In stratiform clouds, $\alpha_v = 3.26 \times 10^7 m^{-1} \cdot s^{-1}$, $b_v = 2$ [17,18].

The number concentration N, median radius R_0, and liquid water content LWC can further be derived from Equations (2)–(4):

$$N = \frac{Z \times \beta^6}{\Gamma(7)} \quad (2)$$

$$R_0 = \frac{3.67}{2\beta} \quad (3)$$

$$LWC = \frac{\pi \rho_c \beta^3 Z \cdot \Gamma(4)}{6\Gamma(7)} \quad (4)$$

where ρ_c is cloud water density, which is set at 10^6 g/m^3.

Doppler velocity V detected by cloud radar is equal to the sum of the mean falling velocity Vm of cloud particles in the stationary atmosphere and the vertical velocity of the ambient atmosphere ω, which can be presented as Equation (5).

$$V = V_m + \omega \quad (5)$$

In stratiform clouds, the mean falling velocity of cloud particles is approximately equal to Equation (6).

$$V_m = \frac{\alpha_v \cdot \Gamma(b_v + 7)}{\beta^{b_v} \Gamma(7)} \quad (6)$$

Re can be derived from R_0 [13,19], as shown in Equation (7).

$$R_e = R_0 \exp\left(\frac{5}{2}\sigma^2\right) \quad (7)$$

where σ is the standard deviation of spectral width, which sets as 0.35.

In addition, the temporal resolution of LC wind profiler data is a 6 min interval; the main data products are wind direction and wind speed; the initial detection height is 150 m; and the vertical resolution is 120 m below 4.1 km. The temporal resolution of meteorological gradient observation is a 5 min interval; the observed variables include several meteorological elements such as atmospheric temperature, humidity, wind direction and speed, amount of precipitation, etc.

The atmospheric circulation background of the process was analyzed by using European Centre for Medium-Range Weather Forecasts Reanalysis v5 data, which is the fifth generation ECMWF atmospheric reanalysis of the global climate covering the period from January 1940 to the present. It mainly includes geopotential height, temperature, sea level pressure, relative humidity, wind field, etc., with hourly temporal resolution and spatial resolution of 0.25° × 0.25°.

3. Inversion of Micro-Physical Parameters of the Sea of Clouds

According to records of the Jiuxian Mountain meteorological station, the sea of clouds case that occurred at 0600-0900BJT on 10 March 2021 has wide spatial coverage with a magnificent viewing effect. The sea of clouds accounts for 80% of the total sky cover, and the cloud top presents a wave-like shape that is 150 m lower than the altitude of the meteorological station. Hereinafter, the micro-physical parameters of the sea of clouds are derived from data from Ka-band cloud radar during the period of time mentioned above.

Figure 2 presents the evolution of the vertically averaged reflectivity factor and liquid water content of the sea of clouds. It can be seen that the overall tendency can be summarized as "thickening–maintenance–dissipation"; hence, this sea of clouds process is divided into the thickening stage (0620-0707BJT), the maintenance stage (0708-0804BJT), and the dissipation stage (0805-0850BJT).

Figure 3 presents the reflectivity factor, Doppler velocity and velocity spectral width, and inversed parameters such as liquid water content, atmospheric vertical velocity, effective radius, and number concentration of cloud particles. During the thickening stage, the echo band greater than −25 dBZ expands gradually (Figure 3a) and liquid water content increases (Figure 3d); meanwhile, uniform updraft changes into a "downdraft on cloud top—updraft at cloud bottom" pattern (Figure 3e), and the effective radius (Figure 3f) and number concentration at the middle part of the cloud body reach their peaks (Figure 3g).

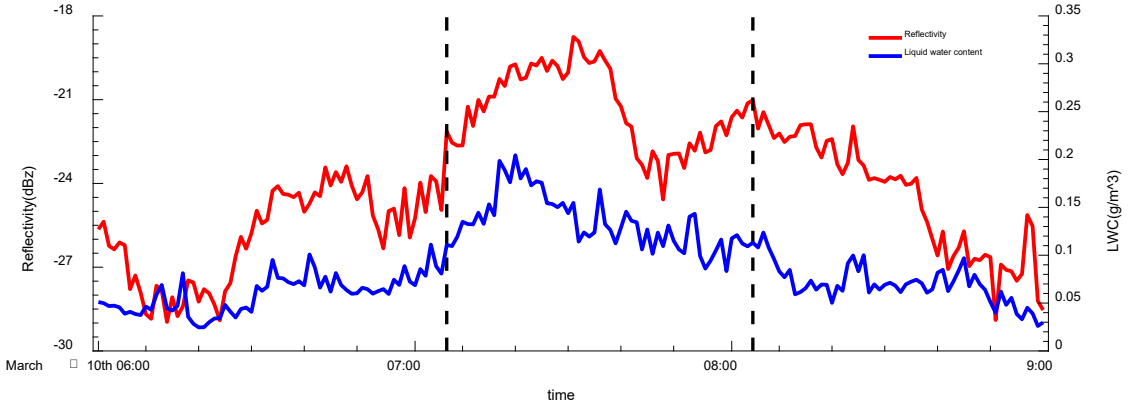

Figure 2. Evolution of vertically averaged reflectivity factor (red line, unit: dBZ) and liquid water content (blue line, unit: g/m^3) during the sea of clouds process from 0600 to 0900 BJT on 10 March.

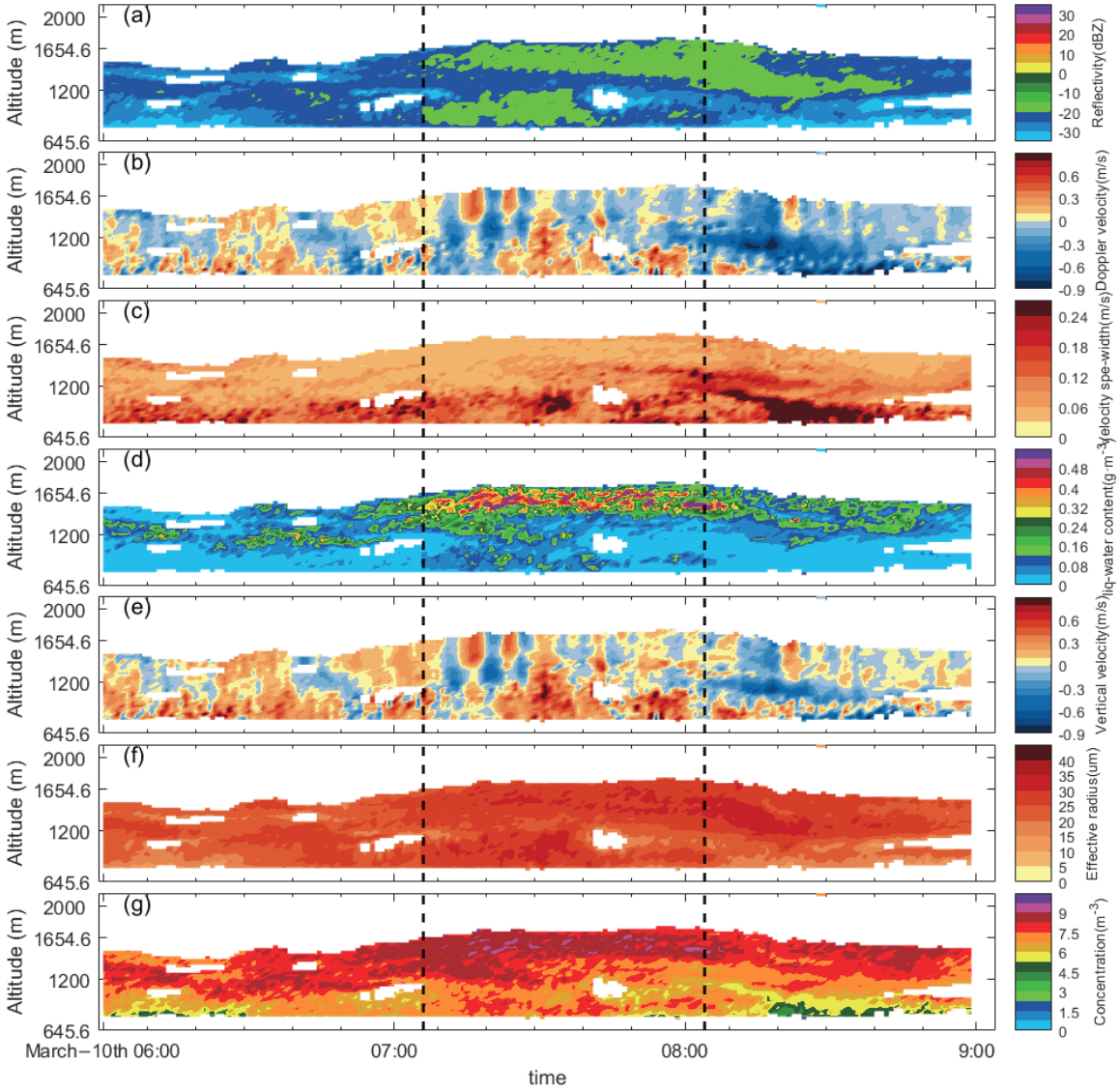

Figure 3. Evolution of variables retrieved from Ka-band cloud radar from 0600 to 0900 BJT on 10 March. Reflectivity factor (**a**), Doppler velocity (**b**), velocity spectral width (**c**), liquid water content (**d**), vertical velocity (**e**), effective radius (**f**), and number concentration (**g**) values are calculated by natural logarithm.

From the 10 min averaged profiles of directly observed and derived variables (Figure 4), the reflectivity factor in the stratiform cloud is about −30~−20 dBZ, a strong echo zone concentrates at the middle and bottom of the clouds, and the velocity spectral width at 1000 m reaches a maximum of 0.18 m/s and reduces to around 0.05 m/s with elevation (Figure 4a). Atmospheric motion within clouds exhibits a "downdraft at cloud top-updraft at cloud bottom" pattern; the high-velocity area at the lower part of the clouds corresponds to the high-velocity spectral width area, which means the updraft at the bottom of the boundary layer is profound and probably results from the turbulence induced by surface friction. Updraft turns into downdraft above 1150 m, and the zero-velocity area is close to the maximum liquid water content (Figure 4b). Strong vertical motion at the boundary layer carries cloud particles upward, which increases the radii of cloud particles through coalescence; thus, the increased gravity partially counteracts the updraft, which weakens the upward motion and results in cloud particles concentrating at this specific height (Figure 4c). At the upper part of the cloud body, the effective radius and liquid water content decrease, presumably because of the entrainment of dry air, whereas the liquid water content slightly increases at the cloud top due to the uplift condensation of small cloud particles with high concentrations.

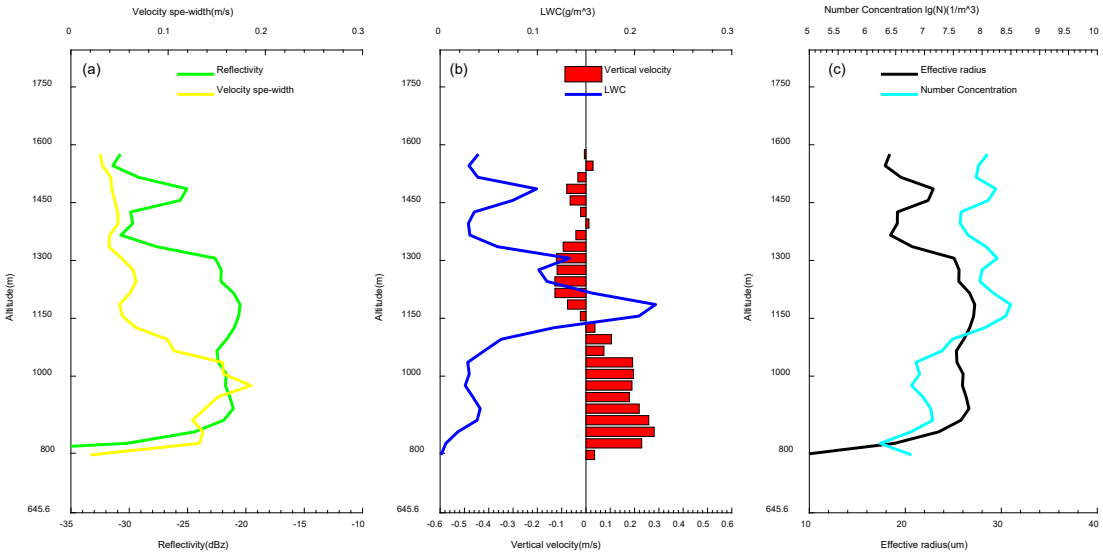

Figure 4. Profiles of averaged reflectivity factor and velocity spectral width (**a**), vertical velocity and liquid water content (**b**), and cloud effective radius and number concentration (**c**) during the thickening stage of the sea of clouds process.

During the maintenance stage, the reflectivity factor persists around −15~−5 dBZ (Figure 5a), the high liquid water content value mainly concentrates at the cloud top (Figure 5b), the vertical motion at the cloud top is alternately updraft and downdraft, which coincides with the wave-like shape of the cloud top, while at the middle part of the cloud body, the vertical motion is "downdraft–updraft–downdraft" and vertical motion at the cloud bottom is still updraft (Figure 5d).

It is worth noting that double strong echo bands exist during 0708-0742BJT; the maximum velocity spectral width at the same time is located at the lower middle part of the cloud body (Figures 5a and 3c), which corresponds to strong upward motion at the bottom of the boundary layer. Small particles are carried up to the middle of the cloud body; therefore, the number concentration in areas with the most intense turbulence significantly decreases and presents as a weak echo band. Parts of cloud particles are dragged down due to the downdraft in the middle of the cloud body, form particles with larger radii through coalescence (Figure 5c) and stagnate at the bottom of the cloud body because of gravity. Updraft at the lower part of the cloud body enhances after 0728BJT, which carries a large amount of cloud particles to the upper part. Subsequently, the echo band at the bottom

of the clouds weakens to −20 dBZ, the vertically averaged reflectivity factor decreases (Figure 2), while the strong echo band at the upper part of the clouds persists; nonetheless, the fluctuation at the cloud top significantly weakens.

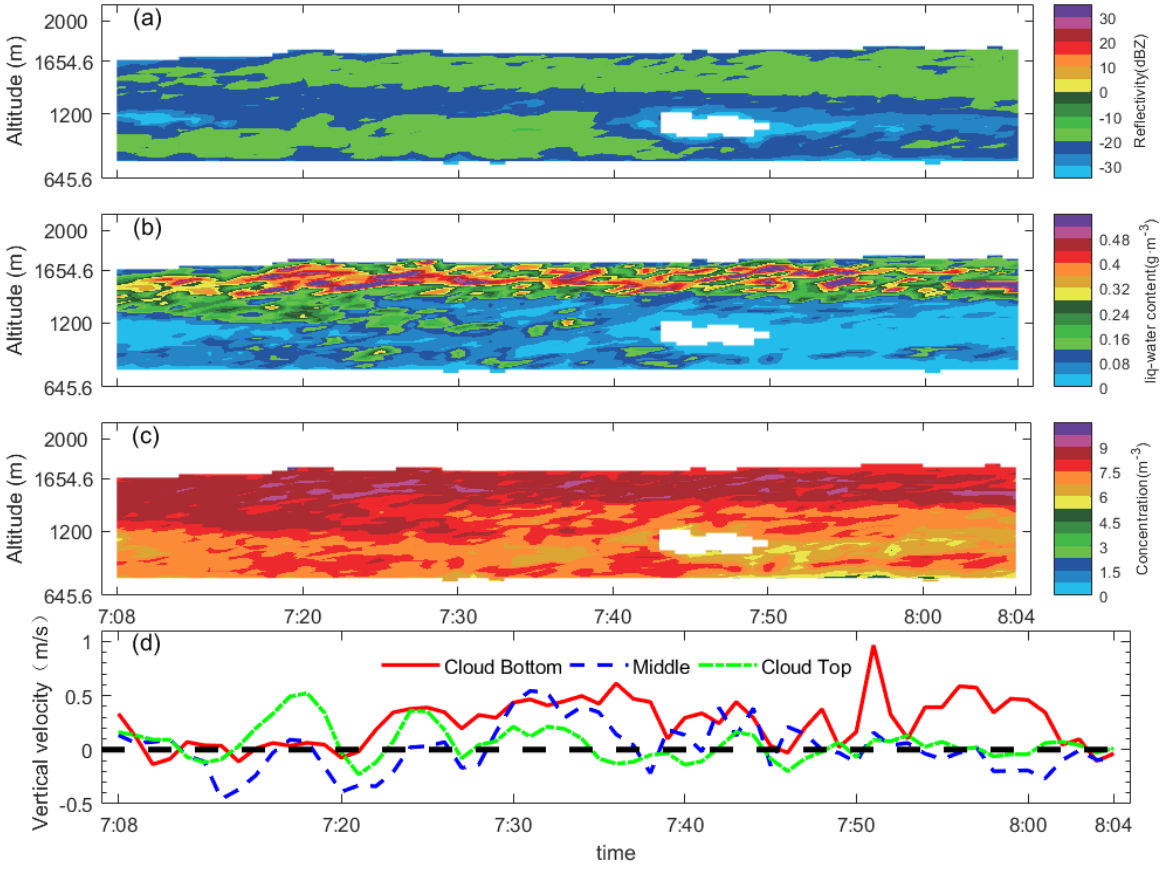

Figure 5. Evolution of variables retrieved from Ka-band cloud radar from 0708 to 0804 BJT [reflectivity factor (**a**), liquid water content (**b**), number concentration (**c**), values are calculated by natural logarithm] and evolution of the vertical velocity (units: m/s) at different levels within the cloud during maintenance stage (**d**): Vertical expansion of the cloud is at the detection depth of 300 to 900 m of cloud radar, with the cloud top located at 900 m indicated by the green line, the cloud bottom located at 300 m indicated by the red line, and the middle level of the cloud body located at 600 m.

During the dissipation stage, a moderately strong echo band (greater than −20 dBZ) descends from the cloud top to the middle part of the cloud body (Figure 6a), the cloud particle liquid water content reduces to 0.08~0.16 g·m^{-3}, the mean Doppler velocity of cloud particles is negative, which means that the dominant motion is downward (Figure 6b). The downdraft in the middle part of the cloud body at this moment is intensified compared to the thickening and maintenance stages. From 10 min averaged (0810-0820BJT) profiles of variables both directly detected and derived from cloud radar, reflectivity factor, velocity spectral width, and others, it can be seen that their features are similar to those of the thickening stage, but downward motion is more distinct and expands to below 1000 m (Figure 6d).

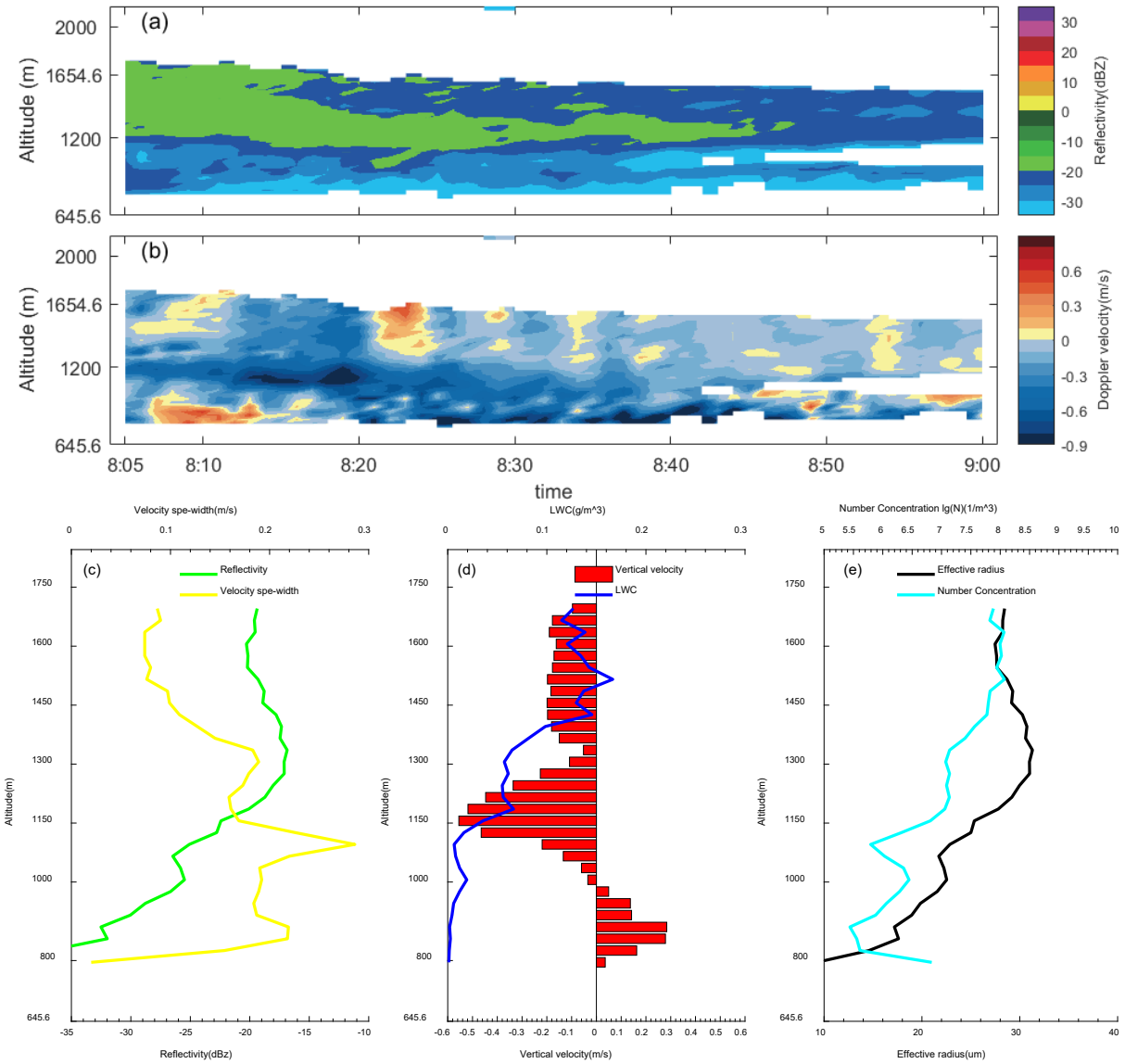

Figure 6. Evolution of variables retrieved from Ka-band cloud radar from 0804 to 0900 BJT. Reflectivity factor (**a**), Doppler velocity (**b**), profiles of averaged reflectivity factor and velocity spectral width (**c**), vertical velocity and liquid water content (**d**), and cloud effective radius and number concentration (**e**) during the dissipation stage of the sea of clouds process.

4. Atmospheric Stratification Feature of the Sea of Clouds

Based on the ERA5 (ECMWF Reanalysis v5) reanalysis data, the evolution characteristics of atmospheric circulation for the sea of clouds case were analyzed from three perspectives: the middle–upper atmosphere, the lower atmosphere, and the boundary layer (Figure 7). From the geopotential height of 500 hPa and the wind field and relative humidity evolution of 700 hPa, there is an upper-air trough entering the Yellow Sea in the middle and high latitudes. The southern branch trough at low latitudes moves eastward with fluctuations, but there is an obvious phase difference with the northern upper-air trough. A shear line appears and is maintained in the middle and lower reaches of the Yangtze River at 700 hPa. With the eastward movement of the southern branch trough, the warm and humid area in the southwesterly airflow in front of the trough gradually expands and develops eastward (Figure 7a–c), and in the lower atmosphere, the central Fujian region gradually changes from the influence of westerly winds to the southwesterly airflow, and with the strengthening of southwesterly airflow, there is a positive temperature change

(Figure 7d–f).But in the boundary layer, due to the influence of cold air over the sea, the northeast airflow is still dominant, and the surface temperature changes negatively (with an increase in sea level pressure) (Figure 7g–i). Under this circulation, the atmospheric stratification in central Fujian during the sea of clouds case is characterized by "middle and lower atmosphere warming, but boundary layer cooling". This is also intuitively reflected in the observation of the meteorological gradient station at Jiuxian Mountain.

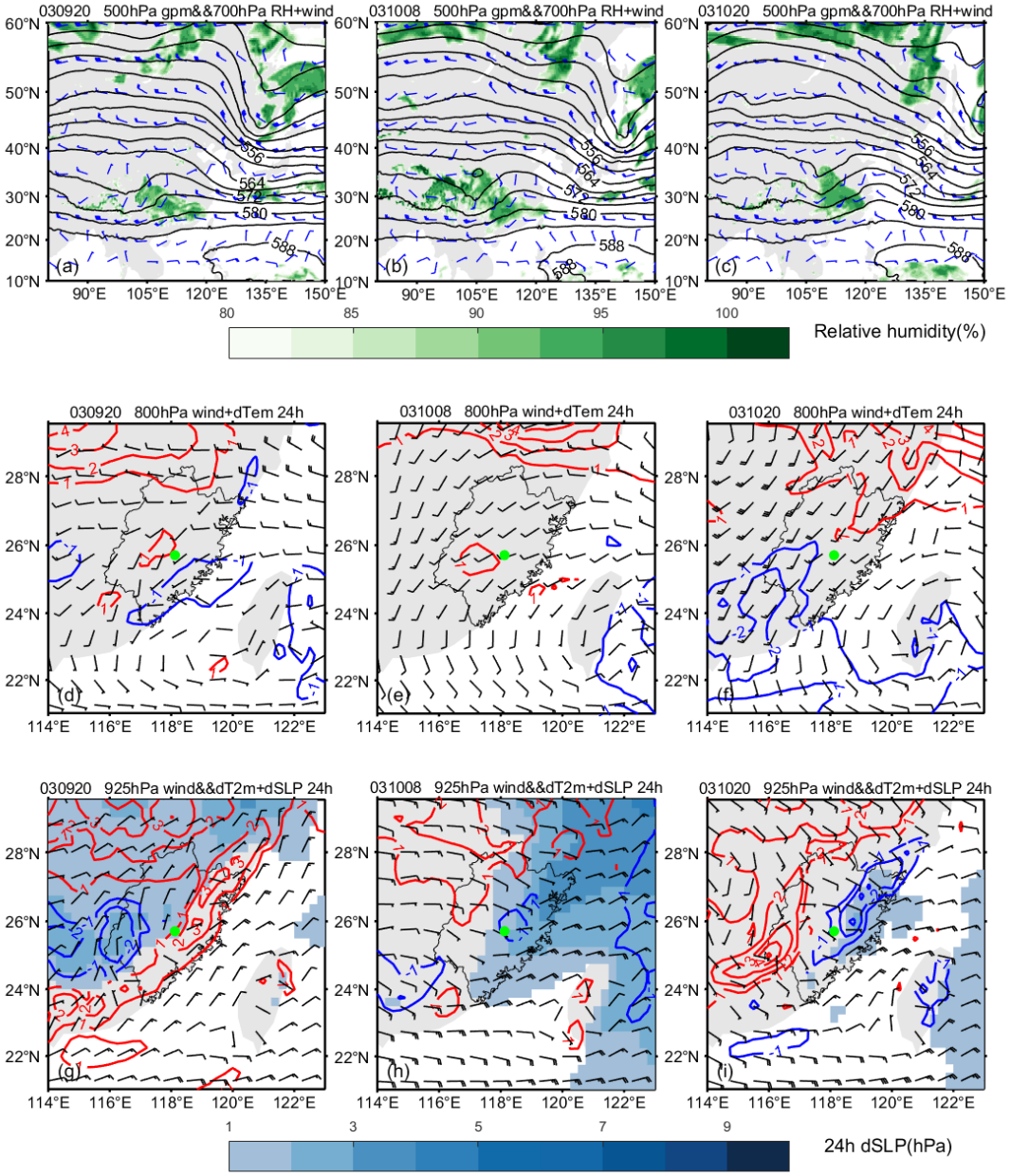

Figure 7. Atmospheric circulation evolution characteristics of the sea of clouds case (from 20:00 on 9 March to 20:00 on 10 March): a geopotential height of 500 hPa (black isoline, units: 10 gpm), a wind field (wind vane units: m/s), and a relative humidity evolution (shading, units: %) of 700 hPa (**a**–**c**); a wind field and variable temperature (isoline, red >0 °C, blue <0 °C) at 850 hPa (**d**–**f**); a wind field of 925 hPa, variable temperature (isoline, red >0 °C, blue <0 °C), and variable Sea level pressure (shading, units: hPa) (**g**–**i**). Green dots in (**d**–**i**) indicate Jiuxian Mountain.

The characteristics of stratification structure are further analyzed using data collected from meteorological gradient stations and LC wind profilers.

From the observation of meteorological gradient stations, during the thickening stage, a weak thermal inversion layer (lapse rate is about −0.05~−0.21 °C/100 m) emerges at 1336–1522 m height (Figure 8a). The bottom of this inversion layer corresponds to the strong echo band (greater than −25 dBZ, Figure 4a). Meanwhile, uniform southeasterly can be seen at 1200–1600 m height during the same period of time from the detection of the wind profiler (Figure 9a). Due to the topography, which is high terrain in the northwest and low terrain in the southeast, the southeasterly slope of the lower level converges at a windward slope, and water vapor condenses into cloud particles. In addition, the maximum refractive index structure constant (hereinafter Cn) usually appears at the cloud top [15,20–23], the maximum inflection point of the Cn profile indicates the detectable cloud top height. The maximum inflection point ascends gradually during the thickening stage, which indicates that the cloud top height increases and the cloud body thickens. Cn reaches its maximum at the later part of the thickening stage (Figure 9b), which demonstrates that intense turbulent activity is the main factor that causes the thickening of the cloud body.

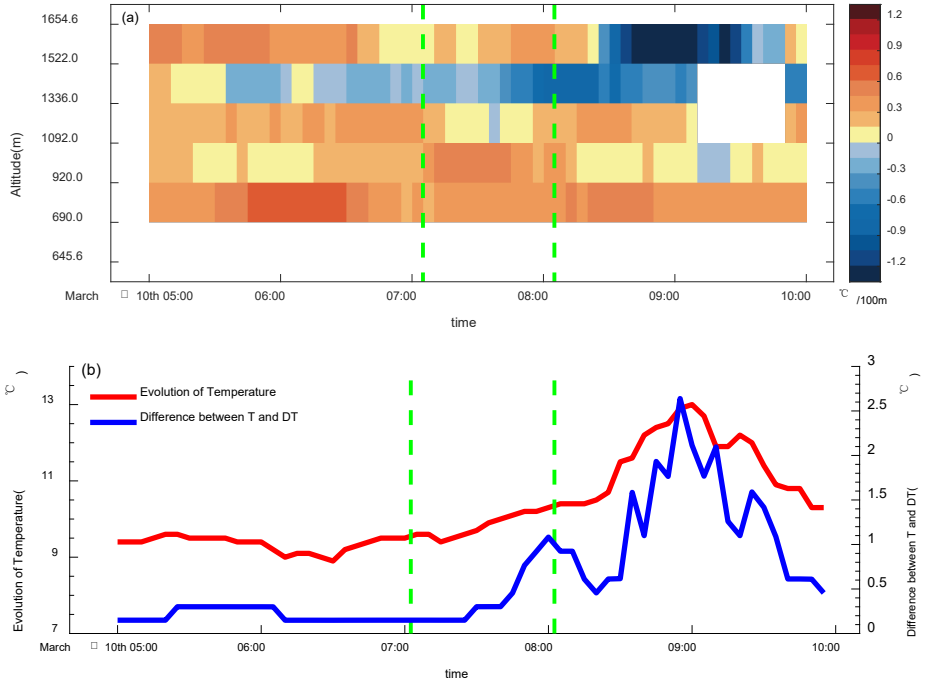

Figure 8. (**a**) Evolution of thermal inversion layer observed by meteorological gradient observation station (shadings indicate atmospheric lapse rate, negatives indicate thermal inversion), evolution of temperature (red line, units: °C). (**b**) Difference between temperature and dew point temperature (blue line, units: °C). The green dashed line is the time node of different phases.

During the maintain stage, the thermal inversion layer at 1336–1522 m height persists and develops slowly (the lapse rate slowly increases to −0.7~0.8 °C/100 m). By this time, the southeasterly slope in the lower level turns to easterly, and the Cn profile indicates a double-peak structure (Figure 9a), which corresponds to the double strong echo bands detected by cloud radar (Figure 4a). The maximum inflection point of Cn descends as a whole. It is worth noting that the maximum Cn decreases suddenly during the early period of the maintenance stage. The weakening of turbulent activity cannot lead to the further development of the cloud body, and, thus, the cloud top is sustained at a certain height.

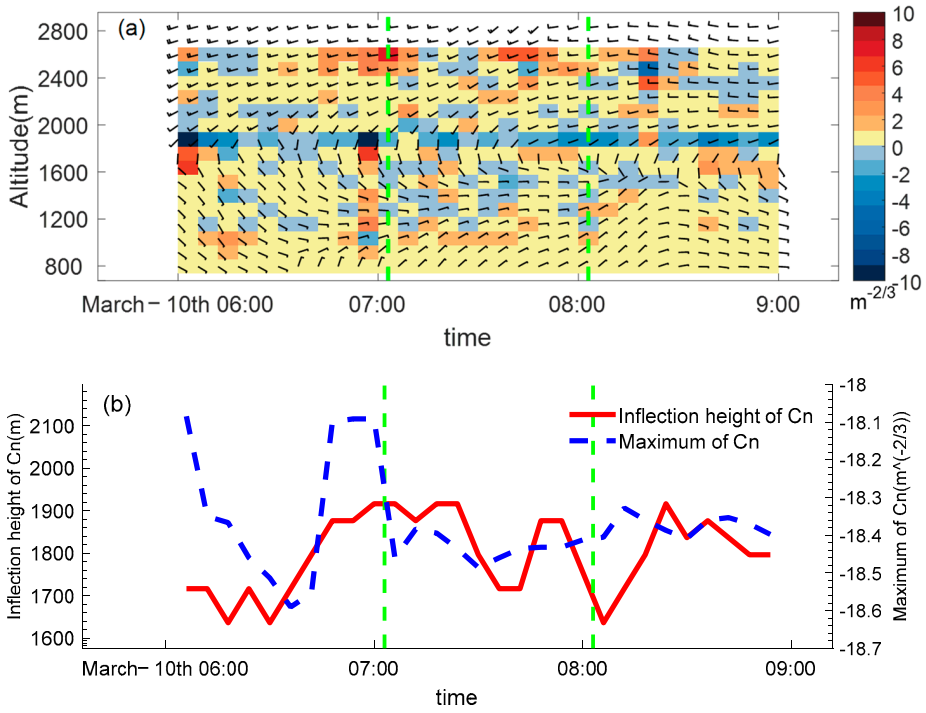

Figure 9. (**a**) Evolution of wind profile detected from wind profiler (barbs, units: m/s) and difference of refractive index structure constant between two adjacent atmospheric layers (shadings, top layer minus bottom layer, positive (negative) means refractive index structure constant increasing (decreasing) with height). (**b**) Evolution of the maximum refractive index structure constant (blue dash line, filtered by moving average) and inflection height (red line, filtered by moving average). The green dashed line is the time node of different phases.

During the dissipation stage, the inversion layer intensifies, the thickness of which increases to the top of Jiuxian Mountain (1654.6 m), the lapse rate increases to greater than −1.2 °C/100 m, the increase in amplitude of temperature at the mountain peak reaches 3.8 °C, the maximum difference between temperature and dew point reaches 2.6 °C (Figure 8b), and the atmosphere tends to be unsaturated. In the meantime, the easterly slope in the lower level changes to northeasterly, and the Cn profile exhibits a single peak structure. The features of the Cn inflection point height and its maximum are similar to those of the maintenance stage, but with a slightly greater maximum value and a higher inflection point height, which means that turbulence within the cloud body is slightly stronger than that of the maintenance stage.

To sum up, the possible formation mechanism of this sea of clouds case could be concluded as follows: First, at the background of the southeasterly slope, turbulence intensifies due to orographic uplift; water vapor condenses into cloud particles through the mixing and entrainment caused by the updraft. As the cloud thickens, the inversion layer is generated by the cooling of evaporation and radiation at the cloud top [24–26]. In return, the updraft is suppressed when the inversion layer at the cloud top intensifies to a certain extent and the vertical motion at the cloud top turns into horizontal advection, which triggers the mixing and entrainment between dry and moist air at the boundary of the cloud body. Sensible heat and latent heat at the cloud bottom transfer to the cloud top by taking turbulence as a carrier, which makes up for the loss of radioactive and evaporative cooling [11,27–30]. As a result, the sea of clouds is maintained; when the radiation from the sun gets stronger, the temperature increase at the cloud top is significantly greater than the cloud bottom because of the absorption of short-wave radiation. The inversion layer thickens and elevates; although the turbulence could be intensified by the heating from the surface, the evaporation of heating outweighs the condensation of cooling, which breaks the balance of compensation, and the cloud body becomes thinner and ultimately dissipates.

5. Conclusions

Based on cloud radar, wind profiler, meteorological gradient observation in high mountains, and other data, the micro-physical characteristics of a typical sea of clouds process in Jiuxian Mountain are investigated by analyzing cloud particle parameters (reflectivity factor, vertical velocity, number concentration, liquid water content of cloud particles, etc.) and atmospheric stratification (temperature, wind, difference between temperature and dew point) features.

(1) According to products from cloud radar, it is found that atmospheric motion within clouds exhibits "downdraft at cloud top-updraft at cloud bottom" during the thickening stage. The zero vertical velocity area is close to the maximum liquid water content, and a weak thermal inversion layer emerges at a height of 1336–1522 m; the bottom of this inversion layer corresponds to the strong echo band. Cloud particles concentrate in the middle of clouds and make the sea of clouds thicker because of the weakening of the updraft.

(2) During the maintenance stage, areas with high liquid water content mainly concentrate at the cloud top, accompanied by alternately upward and downward motion, because of which little cloud particles aggregate and accumulate into clouds, forming a strong and persistent echo band. The thermal inversion layer at 1336–1522 m height persists and develops slowly; by this time, the southeasterly slope in the lower level turns easterly. The Cn profile indicates a double-peak structure, which corresponds to the double strong echo bands detected by cloud radar.

(3) During the dissipation stage, the inversion layer intensifies, the thickness of which increases to the top of Jiuxian Mountain (1654.6 m), a strong echo band descends from the cloud top to the middle part, and the downdraft intensifies compared to the thickening and maintenance stage. Exchanging with dry air is profound due to the unsaturation of water vapor; consequently, the sizes and number concentrations of cloud particles decrease because of the evaporation of cloud particles; a strong echo band gradually narrows down, that is, the cloud body descends and becomes thinner.

However, due to the temporal and spatial inconsistency of multiple source observations and observational devices [31–37] deployed at different locations, this study can only focus on the sea of clouds process with wide coverage, investigate its micro-physical characteristics, and further propose the possible mechanism of the sea of clouds. In fact, clouds and fog formed in the morning and at nightfall are often confined to a small area. Devices in Jiuxian Mountain at present have limited capability to detect a sea of clouds on such a small scale. In addition, sensible heat and latent heat flux caused by radiation or evaporation could not be measured directly; therefore, the formation mechanism concluded in this study may not be suitable for a sea of clouds process occurring under other circumstances.

Author Contributions: Writing—review and editing, S.C.; co-author, writing—original draft, Z.L.; data curation, formal analysis, J.Z.; methodology, Z.L. and G.H.; investigation, Z.C. and Q.Y. All authors have read and agreed to the published version of the manuscript.

Funding: This research was primarily supported by the Natural Science Foundation of Fujian Province of China (Grant No. 2021J01459).

Institutional Review Board Statement: Not applicable.

Informed Consent Statement: Not applicable.

Data Availability Statement: The data presented in this study are available on request from the corresponding author. The data are not publicly available due to privacy.

Conflicts of Interest: The authors declare no conflicts of interest.

References

1. Huang, S.; Yang, X.; Wang, X.; Zhang, X. The Forecast of the Snow Scenery for Tour Weather Service at Lushan Mountain, China. *Meteorol. Mon.* **2007**, *33*, 34–40.

2. Snepenger, D.; Houser, B.; Snepenger, M. Seasonality demand. *Ann. Tour. Res.* **1990**, *17*, 628–630. [CrossRef]
3. Wu, Y.; Wang, K.; Yang, B.; Cheng, T.; Jin, Q.; Wu, J. Synoptic Analysis of a Continuous Cloud Deck Event in Huangshan Mountain, China. *Meteorol. Mon.* **2005**, *31*, 73–76.
4. Zhou, B.; Zhao, J.; Qing, Q.; Yang, S.; Liu, J. Study on Tourism Landscape Snowfall Forecast of Ski Resorts in Xiling Snow Mountain in Autumn and Winter, China. *Plateau Mt. Meteorol. Res.* **2020**, *40*, 74–78.
5. Qiao, S.; Da, Y.; Cao, H. Analysis of time variation and meteorological conditions of Huashan cloud deck, China. *J. Shaanxi Meteorol.* **2016**, 27–30.
6. Fu, B.; Lai, Y.; Wang, W. Analysis of meteorological characteristics and preliminary prediction of cloud deck in Danxia Mountain, China. *Agric. Technol.* **2019**, *39*, 137–140. [CrossRef]
7. Shan, Q.; Feng, G.; Liang, X. Spatial and temporal variation characteristics of the sea of clouds in Yandang Mountain and its relationship with meteorological factors, China. *J. Zhejiang Meteorol.* **2014**, 34–37.
8. Yang, M. *A Study on Retrieving Cloud Microphysical Parameters from Millimeter-Wave Radar Observations, China*; Nanjing University of Information Science and Technology: Nanjing, China, 2019.
9. Shen, F.; Song, L.; He, Z.; Xu, D.; Chen, J.; Huang, L. Impacts of adding hydrometeor control variables on the radar reflectivity data assimilation for the 6–8 August 2018 mesoscale convective system case. *Atmos. Res.* **2023**, *295*, 107–120. [CrossRef]
10. Frisch, A.S.; Lenschow, D.H.; Fairall, C.W.; Schubert, W.H.; Gibson, J.S. Doppler radar measurements of turbulence in marine stratiform cloud during ASTEX. *J. Atmos. Sci.* **1995**, *52*, 2800–2808. [CrossRef]
11. Frisch, A.S.; Feingold, G.; Fairall, C.W.; Uttal, T.; Snider, J.B. On cloud radar and microwave radiometer measurements of stratus cloud liquid water profiles. *J. Geophys. Res. Atmos.* **1998**, *103*, 23195–23197. [CrossRef]
12. Zheng, J.; Liu, L.; Zheng, Z.; Xie, X. Ka-band millimeter wave cloud radar data quality control, China. *J. Infrared Millim. Waves* **2016**, *35*, 748–757.
13. Wei, K.; Huang, X.; Huang, J.; He, H.; Chen, H. Experiment of Retrieving Cloud Micro-physics Parameters by Combining Millimeter-wave Cloud Radar and Ground-based Microwave Radiometer, China. *Sci. Technol. Eng.* **2015**, 8–17. [CrossRef]
14. Zhao, J.; Ma, S.; Dai, T. Analysis and Research on the Detection Capability of Ka-band Millimeter Wave Cloud Radar, China. *J. Chengdu Univ. Inf. Technol.* **2016**, 29–34. [CrossRef]
15. Zhang, K.; Luo, T.; Wang, F.; Sun, G.; Liu, Q.; Qing, C.; Li, X.B.; Weng, N.Q.; Zhu, W.J. Influence of low clouds on atmospheric refractive index structure constant based on radiosonde data, China. *Acta Phys. Sin.* **2022**, *71*, 352–361. [CrossRef]
16. Huang, X.; Lu, L.; Hong, T.; Mei, Y.; Yang, M. A case study on the retrieval of microphysical parameters and in-cloud stratus turbulent dissipation rate by millimeter-wave cloud radar measurement, China. *Trans. Atmos. Sci.* **2020**, *43*, 908–916. [CrossRef]
17. Gossard, E.E. Measurement of cloud droplet size spectra by doppler radar. *J. Atmos. Ocean. Technol.* **1994**, *11*, 712–726. [CrossRef]
18. Gossard, E.E.; Snider, J.B.; Clothiaux, E.E.; Martner, B.; Gibson, J.S.; Kropfli, R.A.; Frisch, A.S. The potential of 8-mm radars for remotely sensing cloud drop size distributions. *J. Atmos. Ocean. Technol.* **1997**, *14*, 76–87. [CrossRef]
19. Atlas, D. The estimation of cloud parameters by radar. *J. Atmos. Sci.* **2010**, *11*, 309–317. [CrossRef]
20. Deng, M.; Mace, G.G. Cirrus microphysical properties and air motion statistics using cloud radar doppler moments. Part I: Algorithm description. *J. Appl. Meteorol. Climatol.* **2006**, *45*, 1690–1709. [CrossRef]
21. Zhang, J.; Chen, H.; Xia, X.; Wei, C.W. Dynamic and thermodynamic features of low and middle clouds derived from atmospheric radiation measurement program mobile facility radiosonde data at Shouxian, China. *Adv. Atmos. Sci.* **2015**, *33*, 21–33. [CrossRef]
22. Sauvageot, H.; Omar, J. Radar Reflectivity of Cumulus Clouds. *J. Atmos. Ocean. Technol.* **1987**, *4*, 264–272. [CrossRef]
23. Zhang, Z.; Xi, S.; Yu, Y. Climatic characteristics and variations of the gelivation weathers in China during 1961–2012, China. *J. Glaciol. Geocryol.* **2015**, *37*, 1435–1442.
24. Zhang, Q.; Xiang, Y.; Wang, Y.; Wang, L.; Lu, C. Research on the Method of Fog Potential Forecast in Fuyang of Anhui, China. *J. Arid Meteorol. Arid Meteorol.* **2015**, *33*, 1045–1049.
25. Zhang, X.; Xu, D.; Li, X. Nonlinear Bias Correction of the FY-4A AGRI Infrared Radiance Data Based on the Random Forest. *Remote Sens.* **2023**, *15*, 1809. [CrossRef]
26. Xu, D.; Zhang, X.; Liu, Z.; Shen, F. All-sky infrared radiance data assimilation of FY-4A AGRI with different physical parameterizations for the prediction of an extremely heavy rainfall event. *Atmos. Res.* **2023**, *293*, 106898. [CrossRef]
27. Matrosov, S.Y. Retrievals of vertical profiles of ice cloud microphysics from radar and IR measurements using tuned regressions between reflectivity and cloud parameters. *J. Geophys. Res. Atmos.* **1999**, *104*, 16741–16753. [CrossRef]
28. Shen, F.; Shu, A.; Liu, Z.; Liu, Z.; Li, H.; Jiang, L.; Zhang, T.; Xu, D. Assimilating FY-4A AGRI Radiances with a Channel Sensitive Cloud Detection Scheme for the Analysis and Forecast of Multiple Typhoons. *Adv. Atmos. Sci.* **2023**, *in press*.
29. Navas-López, J.F.; Darbyshire, R.; Song, X.; Wenden, B.; Close, D. Modelling cherry full bloom using 'space-for-time' across climatically diverse growing environments. *Agric. Forest Meteorol.* **2020**, *284*, 107901. [CrossRef]
30. Li, G. Progress and Prospects in Research of Mountain Meteorology in China During the Past 25 Years, China. *Adv. Meteorol. Sci. Technol.* **2016**, *6*, 115–122.
31. Shen, F.; Min, J.; Xu, D. Assimilation of radar radial velocity data with the WRF Hybrid ETKF–3DVAR system for the prediction of Hurricane Ike (2008). *Atmos. Res.* **2016**, *169*, 127–138. [CrossRef]
32. Shen, F.; Xu, D.; Min, J.; Chu, Z.; Li, X. Assimilation of radar radial velocity data with the WRF Hybrid 4DEnVar system for the prediction of Hurricane Ike (2008). *Atmos. Res.* **2020**, *230*, 104622. [CrossRef]

33. Shen, F.; Xu, D.; Hong, L.; Liu, R. Impact of radar data assimilation on a squall line over the Yangtze-Huaihe River Basin with a radarreflectivity operator accounting for ice-phase hydrometeors. *Meteorol. Appl.* **2021**, *28*, e1967. [CrossRef]
34. Revilloud, M.; Loubier, J.C.; Doctor, M.; Kanevski, M.; Timonin, V.; Schumacher, M. *Artificial Snow Optimization in Winter Sport Destinations Using a Multi-Agent Simulation*; Springer: Berlin/Heidelberg, Germany, 2014; Volume 9, pp. 279–299. [CrossRef]
35. Ding, S.; Duan, W.; Zhu, Y.; Li, G. Forecasting of Hani cloud sea landscape in Yuanjiang county of Yunnan province based on multiple models. *J. Meteorol. Environ.* **2020**, *36*, 106–112. [CrossRef]
36. Zeng, Z.; Zheng, J.; Yang, H.; Zheng, M.; Zeng, Y. Quality control and evaluation on non-cloud echo of Ka-band cloud radar. *J. Appl. Meteorol. Sci.* **2021**, *32*, 347–357. [CrossRef]
37. Shen, F.; Song, L.; Li, H.; He, Z.; Xu, D. Effects of different momentum control variables in radar data assimilation on the analysis and forecast of strong convective systems under the background of northeast cold vortex. *Atmos. Res.* **2022**, *280*, 106415. [CrossRef]